ACS APPLIED MATERIALS & INTERFACES

Research Article

www.acsami.org

Exploiting Differential Electrochemical Stripping Behaviors of Fe_3O_4 Nanocrystals toward Heavy Metal Ions by Crystal Cutting

Xian-Zhi Yao,[†,‡,⊥] Zheng Guo,[†,⊥] Qing-Hong Yuan,[§] Zhong-Gang Liu,[†,‡] Jin-Huai Liu,[†,‡] and Xing-Jiu Huang*[,†,‡]

[†]Nanomaterials and Environmental Detection Laboratory, Hefei Institutes of Physical Science, Chinese Academy of Sciences, Hefei 230031, People's Republic of China

[‡]Department of Chemistry, University of Science and Technology of China, Hefei 230026, People's Republic of China

[§]Department of Physics, East China Normal University, No. 500, Dongchuan Road, Shanghai 200241, People's Republic of China

Supporting Information

ABSTRACT: This study attempts to understand the intrinsic impact of different morphologies of nanocrystals on their electrochemical stripping behaviors toward heavy metal ions. Two differently shaped Fe_3O_4 nanocrystals, i.e., (100)-bound cubic and (111)-bound octahedral, have been synthesized for the experiments. Electrochemical results indicate that Fe_3O_4 nanocrystals with different shapes show different stripping behaviors toward heavy metal ions. Octahedral Fe_3O_4 nanocrystals show better electrochemical sensing performances toward the investigated heavy metal ions such as Zn(II), Cd(II), Pb(II), Cu(II), and Hg(II), in comparison with cubic ones. Specifically, Pb(II) is found to have the best stripping performance on both the (100) and (111) facets. To clarify these phenomena, adsorption abilities of as-prepared Fe_3O_4 nanocrystals have been investigated toward heavy metal ions. Most importantly, combined with theoretical calculations, their different electrochemical stripping behaviors in view of facet effects have been further studied and enclosed at the level of molecular/atom. Finally, as a trial to find a disposable platform completely free from noble metals, the potential application of the Fe_3O_4 nanocrystals for electrochemical detection of As(III) in drinking water is demonstrated.

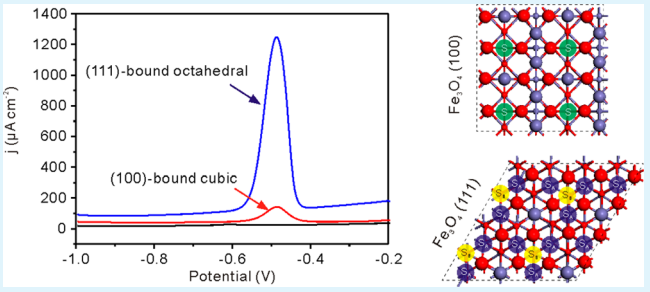

KEYWORDS: *Fe_3O_4 nanocrystals, cubic, octahedral, electrochemical detection, heavy metal ions, theoretical calculations*

INTRODUCTION

In the past several decades, enhanced attention has been paid to the determination of heavy metal ions, because they are extremely harmful in the biosphere and even trace amounts of them pose a detrimental risk to human health.[1−3] Among the current developed approaches, electrochemical analysis, especially the anodic stripping voltammetry method, has been popularly applied due to its short analysis time, portability, low cost, etc.[4−8] To obtain high sensitive and selective detection, various functional materials with the accumulating ability to specific heavy metal ions have been widely reported to modify electrochemical electrodes.[9−15] The basic principle results from the selective interaction of modifiers leads to its selective response, which has been demonstrated in our previous research.[16−18]

Recently, owing to their special chemical and physical properties, nanostructured metal oxides have been widely applied to the adsorption and removal of various heavy metal ions.[19−23] Motivated by this point, they have been employed as promising modifiers of electrochemical electrodes to accumulate heavy meal ions, improving the good sensitivity and selectivity.[24−26] For example, MgO nanoflowers exhibited excellent sensing performance toward Pb(II) and Cd(II) without any interference from other heavy metal ions.[25] Well-arranged porous Co_3O_4 nanosheets presented a high sensitivity and a quite nice low detection limit because of their high adsorption capacities.[27] Especially, by combining the high adsorptivity of Fe_3O_4 microspheres toward As(III), the Fe_3O_4-RTIL (room temperature ionic liquid) composite modified screen-printed carbon electrode showed even better electrochemical performance, e.g., sensitivity reaches 4.91 μA ppb^{-1}, than commonly used noble metals. Under the optimized conditions, it offered direct detection of As(III) within the desirable range (10 ppb) in drinking water as specified by the World Health Organization (WHO). Undoubtedly, their sensing performances can be greatly enhanced through employing the nanostructured metal oxide. However, different from organic functional carbon nanotubes and other modifiers, nanostructured metal oxides have no organic groups selectively complexing with heavy metal ions. Their enhancing effects are

Received: March 17, 2014
Accepted: July 11, 2014
Published: July 11, 2014

generally ascribed to an increased microscopic surface area.[18−20,28] And not enough information on scientifically understanding their enhancing sensing effect could be found.

Actually, single-crystal nanomaterials with different morphologies are exposed with distinct facets, exhibiting specific physical and chemical properties.[29−33] Typically, controlling the shape and thus facets of nanocrystals can manipulate their performance in catalytic reactions. For example, Co_3O_4 nanosheets with exposed (112) facets exhibited enhanced catalytic activity for methane combustion than Co_3O_4 nanobelts with (011) facets and nanocubes with (001) facets.[34] Similar effects have also been extended to electrocatalytic behaviors of nanomaterials. Zhu et al. experimentally reported that the peroxidase-like activities of Fe_3O_4 nanocrystals were structure dependent and followed the order cluster spheres > triangular plates > octahedral.[35] Obviously, the above-mentioned surface catalytic activities could be specifically manipulated by distinct crystallographic facets, which is intrinsically arised from atom arrangement manners and dangling bonds on the exposed surface.[36−39]

The surface interaction, as a critical step, is inevitably involved in the electrochemical detection of heavy metal ions at the modified electrodes. Initiated from this view, we envisage that electrochemical stripping behaviors of heavy metal ions could depend on their interactions with the surfaces of modified nanomaterials, meaning that it is also controlled by the effect of crystal facets. To demonstrate this idea, herein two differently shaped Fe_3O_4 nanocrystals has been prepared and their stripping behaviors toward heavy metal ions have been carefully investigated in experiment and theory. First, cubic and octahedral nanocrystals Fe_3O_4 have been prepared, which are exposed with (100) and (111) facets, respectively. Electrochemical stripping behaviors of heavy metal ions, e.g., Pb(II), Zn(II), Cd(II), Cu(II), and Hg(II), on both cubic and octahedral Fe_3O_4 nanocrystals were thoroughly investigated. Adsorption experiments of cubic and octahedral Fe_3O_4 nanocrystals toward the five mentioned metal ions were carried out to assess the adsorption capacity of Fe_3O_4 nanocrystals. Theoretical computations by density functional theory (DFT) were performed to demonstrate the surface interaction between the heavy metal ions and different facets and to further understand the different stripping behaviors. The results will provide important insights into the broad impacts of exposed facets of nanocrystals on the increased electroanalytical performances of nanostructured materials.

EXPERIMENTAL SECTION

Chemical Reagents. All chemicals were of analytical grade and used as received without any further purification from Sinopharm Chemical Reagent Co., Ltd. (China). Stock solutions of Zn(II), Cd(II), Pb(II), and Cu(II) were prepared by dissolving $Zn(NO_3)_2{\cdot}6H_2O$, $3CdSO_4{\cdot}8H_2O$, $Pb(NO_3)_2$, and $Cu(NO_3)_2$ in deionized (DI) H_2O, respectively. Hg(II) was prepared by dissolving $Hg(NO_3)_2$ in DI H_2O assisted by several drops of HNO_3. Acetate buffer solutions of 0.1 M with different pH were prepared by mixing stock solutions of 0.1 M NaAc and HAc. Phosphate buffer solutions (PBS) of 0.1 M were prepared by mixing stock solutions of 0.1 M H_3PO_4, KH_2PO_4, K_2HPO_4, and NaOH. NH_4Cl−$NH_3{\cdot}H_2O$ (0.1 M) solution was prepared by mixing stock solutions of 0.1 M NH_4Cl and $NH_3{\cdot}H_2O$ in different proportions. All solutions were prepared with DI H_2O of resistivity not less than 18.2 MΩ cm.

Preparation of Cubic and Octahedral Fe_3O_4 Nanocrystals. In a typical synthesis of cubic Fe_3O_4 crystals similar to a previous report,[40] $FeSO_4{\cdot}7H_2O$ (2.5 mmol) was dissolved into DI H_2O (30 mL) under vigorous stirring. Then, $N_2H_4{\cdot}H_2O$ (5 mL, 55 vol %) was added under a blanket of N_2. Subsequently, the pH value of the solution was adjusted to 11 by dropping a certain amount of KOH solution (5 M). Finally, the above solution was transferred into a Teflon-lined stainless-steel autoclave of 50 mL capacity and sealed to heat at 200 °C for 24 h. After the reaction and naturally cooling to room temperature, the products were obtained. For synthesis of octahedral Fe_3O_4 nanocrystals, a mild hydrothermal approach was employed without involving any surfactants. Briefly, $FeSO_4{\cdot}7H_2O$ (2.5 mmol) was dissolved into DI H_2O (80 mL). Following the addition of 2.0 M KNO_3 (10 mL) and 1.0 M NaOH (10 mL), the solution in an oxygen-free environment was stirred at 40 °C for 8 h, which leads to the formation of octahedral Fe_3O_4 nanocrystals. At last, all obtained products were washed with water and ethanol for several times and then dried in a vacuum at 60 °C.

Fabrication of Modified Electrochemical Electrodes. Prior to modification, the glassy carbon electrode (GCE, diameter of 3 mm) was sequentially polished with 0.3 and 0.05 μm alumina powder slurries to a mirror shiny surface and successively sonicated with 1:1 (V/V) HNO_3 solution, ethanol, and DI water to remove any adsorbed substances on its surface. As-prepared cubic or octahedral Fe_3O_4 nanocrystals (4 mg) were dissolved into ethanol (1 mL) and sonicated to obtain a homogeneous suspension. Then, the above suspension (3 μL) was dropped onto the fresh surface of GCE. With the solvent completely evaporated at room temperature, cubic or octahedral Fe_3O_4 nanocrystals modified electrodes were obtained.

Electrochemical Experiments. Square wave anodic stripping voltammetry (SWASV) was used for the electrochemical detection. First, the modified electrode was immersed in a 10 mL solution containing heavy metal ions for a certain time (20 min) in an open circuit. During preconcentration, the solution was efficiently stirred. Then the electrode was carefully washed with DI H_2O and kept in the cell containing 10 mL of supporting electrolyte solution. A negative potential of −1.0 V (−1.4 V for Zn(II)) was immediately applied for 120 s to completely reduce the adsorbed heavy metal ions in 0.1 M NaAc−HAc (pH = 5). Subsequently, the anodic stripping (reoxidation of metal to metal ions) was performed in a certain potential range with a frequency of 10 Hz, amplitude of 25 mV, and step potential of 4 mV.

Adsorption Experiments. Adsorption was carried out using a 25 mL Erlenmeyer flask containing 10 mg of adsorbents and 0.1 mM aqueous solutions of heavy metal ions at room temperature, which was continuously stirred for 24 h. Then the adsorbents were separated by centrifugation. The concentration of heavy metal ions remaining in the solution was analyzed using inductively coupled plasma atomic emission spectrophotometry (ICP-AES) (Thermo Fisher Scientific, model ICP 6300).

Computational Details. First principle calculations were performed to investigate the adsorption ability of different metal ions on the Fe_3O_4 (100) and (111) surfaces. All calculations were performed within the framework of density functional theory (DFT), as implemented in the Vienna ab-initio simulation package (VASP).[41,42] Electronic exchange and correlation are included through the generalized gradient approximation (GGA) in the Perdew−Burke−Ernzerhof (PBE) form.[43] The projector-augmented wave (PAW) method is used to describe the electron interaction and the plane-wave kinetic-energy cutoff is set as 400 eV. The most stable (100) and (111) surface was used as the adsorption surfaces. The lattice parameters of each surface unit cell are chosen according to the corresponding optimized bulk parameters. The supercell of the slab model is composed of 2 × 2 repeating unit cells and the 2 × 2 × 1 k-point mesh is used for the calculation. After the adsorbed structures are set up, an optimization of the atomic positions is performed for each structure under the restriction of fixed lattice parameters and fixed three bottom layers. The ground state geometries are obtained by minimizing the forces on each atom to become less than 0.02 eV/Å. Adsorption energy, E_{ads}, of each metal atom adsorbing on the surfaces is defined as $E_{ads} = E_{ads\text{-}slab} - (E_{slab} + E_{metal\ atom})$, where $E_{ads\text{-}slab}$ is the total energy of the slab interacting with metal atom; E_{slab} is the total energy of bare slab; $E_{metal\ atom}$ is the energy of one metal atom in the

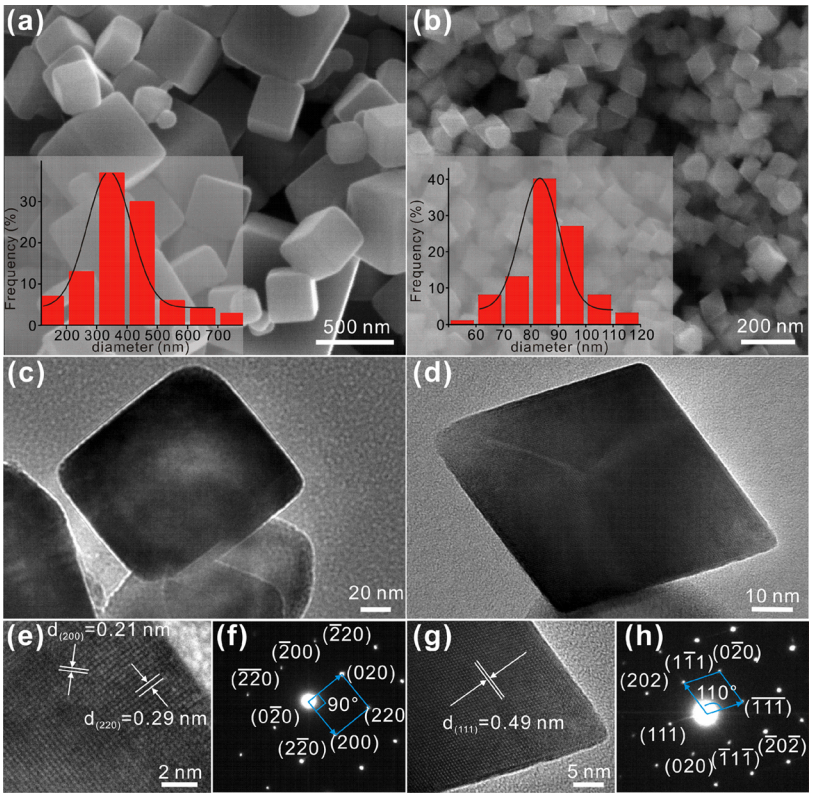

Figure 1. SEM images of Fe_3O_4 nanocrystals: (a) cubic, (b) octahedral; the insets in (a) and (b) are the corresponding distribution of their particle sizes. TEM images of Fe_3O_4 nanocrystals: (c) cubic, (d) octahedral. HRTEM images of Fe_3O_4 nanocrystals: (e) cubic, (g) octahedral. SAED patterns of Fe_3O_4 nanocrystals: (f) cubic, (h) octahedral.

vacuum. Therefore, the more negative the E_{ads}, the stronger the interaction of heavy metal with the Fe_3O_4 surface.

Apparatus. Electrochemical experiments were recorded using a CHI 660D computer-controlled potentiostat (ChenHua Instruments Co., Shanghai, China) with a standard three-electrode system. A bare or modified GCE served as a working electrode; a platinum wire was used as a counter electrode with a saturated Ag/AgCl electrode (SCE, ChenHua Instruments Co., Shanghai, China) completing the cell assembly.

The morphologies of the as-prepared samples were investigated by scanning electron microscopy (SEM, Quanta 200 FEG, FEI Company, USA). Transmission electron microscopy (TEM) and high-resolution TEM (HRTEM) analyses were performed using a JEM-2010 transmission electron microscope operated at 200 kV (quantitative method: Cliff–Lorimer thin ratio section).

RESULTS AND DISCUSSION

Characterization of Fe_3O_4 Nanocrystals. Fe_3O_4 nanocrystals with cubic and octahedral morphologies have been prepared via a similar hydrothermal method without involving any surfactants, the SEM images are shown in Figure 1a,b. It is seen that as-synthesized Fe_3O_4 nanocrystals present regular cubic and octahedral structures, respectively. The distributions of their particle sizes are uniform, which can be inferred from the insets of Figure 1a,b, respectively. For cubic nanocrystals, it is mainly distributed in the range of 350–450 nm, which is larger than 85–95 nm of octahedral ones. It is important to mention that the adsorption difference at a level of tens of nanometers to hundreds of nanometers could be ignored,[44] that is, we do not need to consider the size effect in the following study. TEM images shown in Figure 1c,d further demonstrate that as-synthesized Fe_3O_4 nanocrystals are with perfect cubic and octahedral morphologies. On the basis of the HRTEM image (Figure 1e) and SAED pattern (Figure 1f), evidently as-prepared cubic nanocrystals is a single-crystalline structure exposed with the (100) facet. The adjacent lattice fringe spacing of about 0.21 and 0.29 nm correspond to the (200) and (220) facets of Fe_3O_4 nanocrystals, respectively.[40,45] For octahedral nanocrystals, they are also with the single-crystalline structure. Different from cubic one, octahedral Fe_3O_4 nanocrystals are enclosed with (111) facet, which can be concluded from its HRTEM image (Figure 1g) and SAED pattern (Figure 1h). The adjacent lattice fringe spacing of about 0.49 nm corresponds to the (111) facet of the Fe_3O_4 nanocrystals. To further characterize the composition of as-prepared samples, their X-ray diffraction (XRD) patterns have been performed and shown in Figure 2. It can be seen that XRD pattern of cubic nanocrystals is identical to octahedral ones. They are both indexed to that of Fe_3O_4 with face-centered-cubic structure (JCPDS card No. 65-3107). Moreover, no diffraction peaks of any other phases can be observed, indicating the high purity of as-prepared products is obtained. The strong and sharp diffraction peaks further reveal that as-synthesized Fe_3O_4 cubic and octahedral nanocrystals are both well crystallized. Details for synthesis and BET results could be seen in the Supporting Information (Figures S1–S4).

Stripping Behaviors of Heavy Metal Ions on Fe_3O_4 Nanocrystals. Prior to the stripping experiments, the modified electrodes were basically characterized using cyclic voltammograms and Nyquist diagram of electrochemical impedance spectra (Supporting Information, Figures S5 and S6), and optimization of electrochemical conditions was seen in Figure S7 (Supporting Information). SWASV curves toward various concentrations of Pb(II) on cubic and octahedral Fe_3O_4

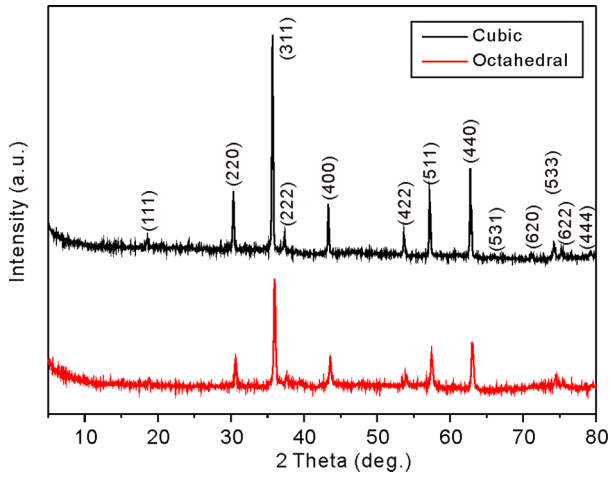

Figure 2. XRD patterns of as-synthesized cubic and octahedral Fe_3O_4 nanocrystals. X-ray diffraction (XRD) patterns were recorded with a Philips X'Pert X-ray diffractometer, using Cu Kα ($\lambda_{K\alpha 1}$ = 1.5418 Å) as the radiation source.

nanocrystals modified electrodes have been performed (Figure 3). Clearly, it can be observed that octahedral Fe_3O_4 nanocrystals have a much higher sensitivity and lower limit of detection toward Pb(II) than that of cubic Fe_3O_4 nanocrystals. The more positive shift of the peaks shown in Figure 3a should

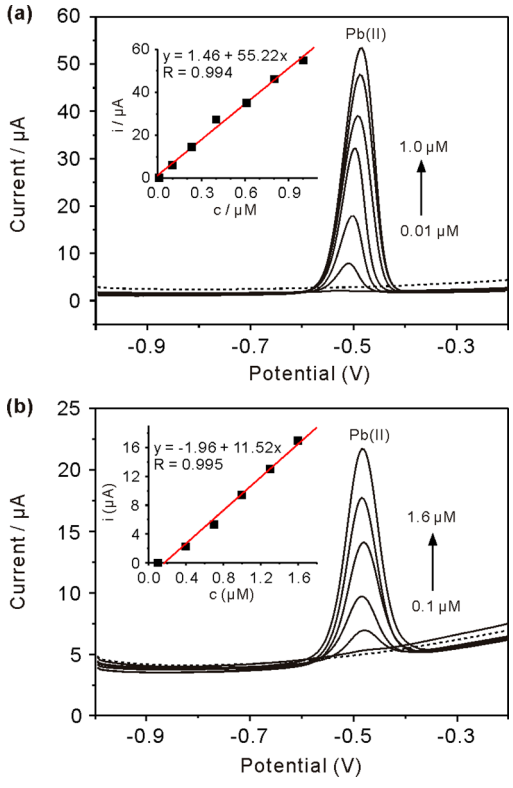

Figure 3. Typical SWASV response of (a) octahedral and (b) cubic Fe_3O_4 nanocrystals modified GCE for determination of Pb(II). Insets are the corresponding linear calibration plots of peak current against concentrations. Supporting electrolyte, 0.1 M acetate buffer (pH 5.0); accumulation time, 20 min; reduction potential, −1.0 V; reduction time, 120 s; amplitude, 25 mV; increment potential, 4 mV; frequency, 50 Hz. The dotted line refers to the baseline.

be ascribed to the consequence of the overlap of diffusion layers produced from the stripping of the Pb(0) to Pb(II).

Figure 4a shows that the stripping peak currents at about −0.49 V are greatly enhanced on the modified electrode.

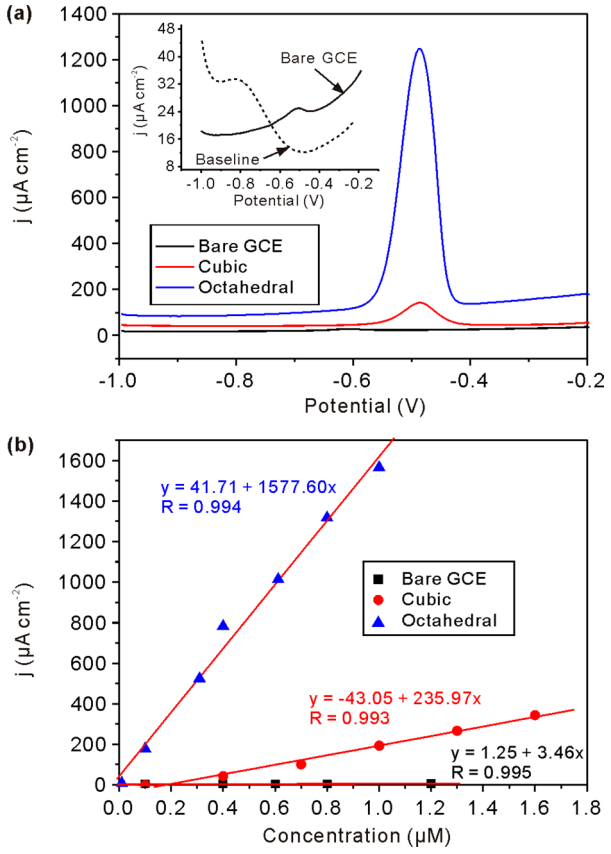

Figure 4. (a) Typical SWASV responses of 1.0 μM Pb(II) at bare (black line), cubic Fe_3O_4 nanocrystals (red line), and octahedral Fe_3O_4 nanocrystals (blue line) modified GCE in 0.1 M NaAc−HAc solution (pH = 5.0). Inset is an enlarged SWASV response of 1.0 μM Pb(II) at bare GCE. The dotted line is the baseline. (b) Corresponding linear calibration plots of peak current density against concentrations of Pb(II).

However, at bare GCE, it only presents a weak response, which can be neglected. Interestingly, the response of octahedral nanocrystal modified electrode is much better than that on cubic ones. As seen from the comparison of calibration plots of Pb(II) shown in Figure 4b, the peak current densities increased linearly versus the Pb(II) concentrations with a sensitivity of 235.97 μA cm^{-2} μM^{-1} for cubic nanocrystals and 1577.60 μA cm^{-2} μM^{-1} for octahedral ones, which are much higher than that of bare GCE (3.46 μA cm^{-2} μM^{-1}). The results indicate that Fe_3O_4 nanocrystals employed to modify GCE greatly improve the sensing performances to Pb(II). And (111)-bound octahedral Fe_3O_4 nanocrystals exhibit better electrochemical performances than (100)-bound cubic Fe_3O_4 nanocrystals. Notably, it is clear that the Fe_3O_4 nanocrystals modified electrodes show essentially the same stripping peak so that the metal is stripped from the electrode surface in all cases (and not from the surface of the iron oxides). The role of the iron oxides is to increase the size of the signal but not change its nature (its stripping is from the electrode as above, see inset in Figure 4a). This likely happens via preconcentration of the target ions on the iron oxides (via reversible adsorption onto the iron oxides)

and then when a negative potential is applied to the electrode these ions move from the iron oxide (desorb) and become plated as lead on the electrode. Then when the stripping sequence is applied, larger signals are seen. Thus, the different signals reflect different extents of adsorption of Pb(II) on the different crystal faces, as will be carefully discussed by the following adsorption experiments and theoretical calculations.

Besides Pb(II), the analytical performances of (100)-bound cubic and (111)-bound octahedral Fe_3O_4 nanocrystals toward other metal ions, such as Zn(II), Cd(II), Cu(II), and Hg(II) were systematically compared, as shown in Figure 5. Their

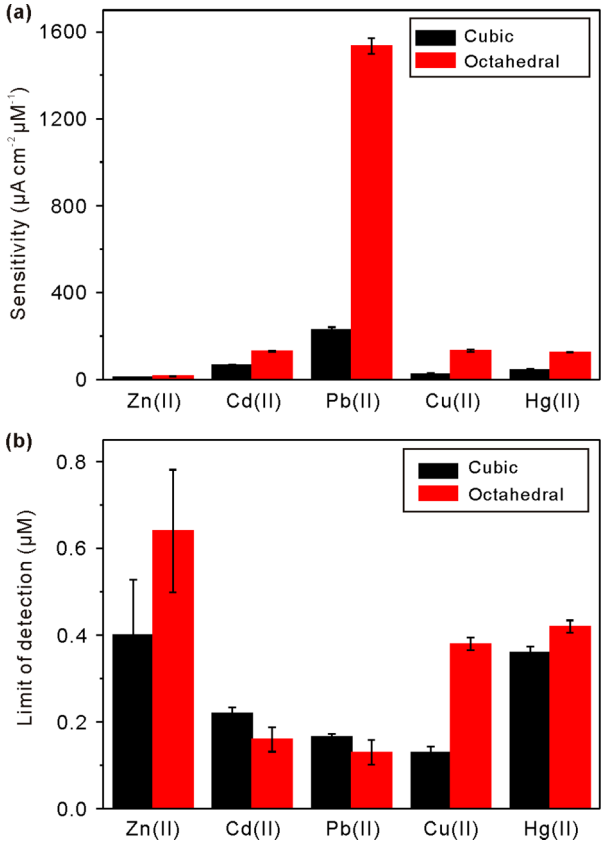

Figure 5. Comparison of (a) sensitivity and (b) limit of detection (3σ method) for SWASV detection of Zn(II), Cd(II), Pb(II), Cu(II), and Hg(II) at Fe_3O_4 cubic and octahedral nanocrystals, respectively.

corresponding SWASV responses and linear calibration plot can be found in the Supporting Information, Figures S8 and S9. Different from stripping behaviors of Pb(II), all of them present weaker stripping peaks with lower sensitivities. First, the sensitivities of Zn(II), Cd(II), Cu(II), and Hg(II) on cubic Fe_3O_4 nanocrystals shown in Figure 5a are about 10.20, 64.08, 24.29, and 40.41 $\mu A\ cm^{-2}\ \mu M^{-1}$, respectively. And their limits of detection (LODs) are about 0.31, 0.21, 0.12, and 0.35 μM, respectively (Figure 5b). Obviously, the cubic nanocrystals modified GCE shows the best response for Pb(II) among all investigated heavy metal ions. Second, through exploring the stripping behaviors of heavy metal ions on octahedral Fe_3O_4 nanocrystals modified GCE, similar results have also been obtained that it shows the best response to Pb(II), which can be demonstrated from the sensitivity of Zn(II), Cd(II), Cu(II), and Hg(II) shown in Figure 5a. Their sensitivities are about 14.57, 126.57, 128.00, and 126.29 $\mu A\ cm^{-2}\ \mu M^{-1}$, respectively, which is lower than that of Pb(II). Furthermore, the LODs on (111)-bound octahedral nanocrystals are about 0.74 (Zn(II)), 0.14 (Cd(II)), 0.39 (Cu(II)), and 0.43 (Hg(II)) μM, respectively (Figure 5b). It is easy to find that stripping behaviors of metal ions on (111)-bound octahedral nanocrystals are superior to that on (100)-bound cubic nanocrystals.

As discussed above, the nature of increased stripping signal is via reversible adsorption of the target ions onto the iron oxides' surface. To make sure the contribution of the adsorption, their adsorption capabilities of cubic and octahedral Fe_3O_4 nanocrystals toward different heavy metal ions have been addressed, the results are shown in Figure 6. Here the adsorption capacity

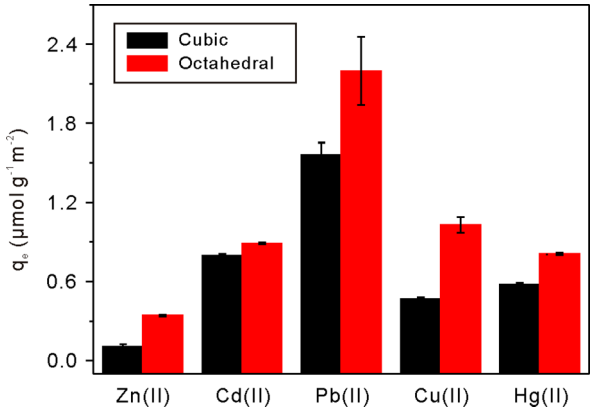

Figure 6. Adsorption of cubic and octahedral Fe_3O_4 nanocrystals for 0.1 mM Zn(II), Cd(II), Pb(II), Cu(II), and Hg(II). Adsorbent dose = 1 $g \cdot L^{-1}$; solvent, H_2O, pH = 7.0 ± 0.2; shaking rate = 100 rpm; contact time = 24 h; T = 298 K.

of cubic and octahedral Fe_3O_4 nanocrystals was calculated with the correction of specific surface area to eliminate the effect of surface area. As seen, adsorption capacity of Fe_3O_4 nanocrystals for different metal ions is quite distinguishing. Both cubic and octahedral Fe_3O_4 nanocrystals present the highest adsorption capacity toward Pb(II), which is well in agreement with its best response on their modified electrodes. Moreover, octahedral Fe_3O_4 nanocrystals show a higher adsorption capacity than cubic nanocrystals for any metal ions. It can be concluded that the adsorption performances of the Fe_3O_4 nanocrystals to heavy metal ions are in agreement with their electrochemical behaviors.

Theoretical Calculations. To further understand how the facets of Fe_3O_4 nanocrystals affect the adsorption behavior of metal ions, we performed density functional theory (DFT) calculations to explore the adsorption energies of Zn, Cd, Pb, Cu, and Hg atoms on Fe_3O_4(100) and (111) surfaces. The adopted computational models are similar to the recent report on Li storage capability of Ti_3C_2 and $Ti_3C_2X_2$ (X = F, OH) monolayers.[46] The most stable surfaces, as shown in Figure 7, were selected as typical Fe_3O_4(100) and (111) surface, respectively. After geometry optimizations, the most favorable adsorption site on the (100) surface is shown in Figure 7a, marked by S, whereas two favorable adsorption sites (marked by S_A and S_B) can be identified on (111) surface (Figure 7b). This can be attributed to the different atomic structure of Fe_3O_4 (100) and (111) surfaces.[47−49] It is well-known that metal atoms prefer to bind with the O atom of the Fe_3O_4 surface. Although both (100) and (111) surfaces have 16 surface oxygen atoms in each supercell, the site provided for the heavy metal atom adsorption is quite different because of the

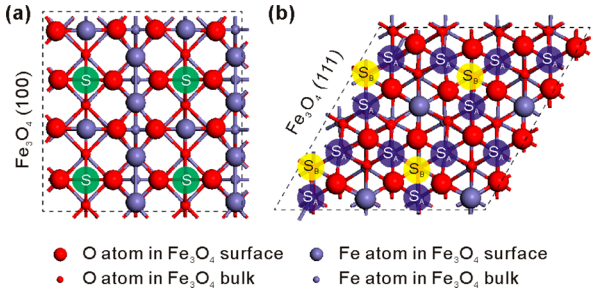

Figure 7. Possible adsorption sites on (a) cubic and (b) octahedral Fe_3O_4 nanocrystals. S, adsorption sites of heavy metal ions on Fe_3O_4 (100) facet; S_A and S_B, two kinds of adsorption sites of heavy metal ions on the Fe_3O_4 (111) facet.

different number of surface Fe atoms. On the (100) surface, there are 12 Fe atoms that occupied most of the adsorption sites, but there are only 4 surface Fe atoms on the (111) surface. Hence, there are four adsorption sites on the (100) facets, whereas there are 12 adsorption site S_A and four adsorption site S_B on the (111) facets, as shown in Figure 7. It can be deduced that, within the same surface area, the adsorption site on the (111) facet is much more than that on the (100) facet. Accordingly, the number of adsorption sites on the exposed surfaces will contribute to the adsorption capacity of heavy metal ions, which further affects their electrochemical stripping behaviors.

Besides the adsorption site, the adsorption energies of different metal atoms on the Fe_3O_4 (100) and (111) surfaces are also quite different. Table 1 lists the calculated adsorption energies of different heavy metal atoms on the (100) and (111) facets. As seen, among all the considered heavy metal atoms, Pb has the largest adsorption energy on both Fe_3O_4 (100) and (111) surfaces. That is, the adsorption energies of Pb on the (100) and (111) facets are −3.01 and −3.65/−3.64 eV, respectively. For Zn, Cd, and Hg atoms, the adsorption energies are quite small on both the (100) and (111) facets, demonstrating a weak or nonadsorption. This calculation result is quite consistent with our experimental observations: Pb shows the highest adsorption capacity on both the (100) and (111) facets and also represents better electrochemical sensing performance than Zn, Cd, and Hg. An exception case is for Cu, where theoretical calculations demonstrated its moderate adsorption ability but weak electrochemical sensing ability was observed in our experiment. This can be explained from the Cu−O bond length observed from Figure 8, which is 1.969/1.993 Å. The short bond length makes it more easily adsorbed onto Fe_3O_4 nanocrystals. Nevertheless, not only adsorption ability has great influence on electrochemical performance but also desorption ability. The weaker desorption ability has hindered its redeposit process and even affected electrochemical stripping behaviors.

Table 1. Adsorption Energy (eV) of Heavy Metal Ions on Cubic and Octahedral Fe_3O_4 Nanocrystals[a]

		Fe_3O_4 (111)	
heavy metal ions	Fe_3O_4 (100)	S_A	S_B
Cd	−0.27	0.03	−0.04
Cu	−2.08	−2.09	−2.13
Hg	0.09	−0.16	0.48
Pb	−3.01	−3.65	−3.64
Zn	−0.49	−0.69	−0.65

[a] S_A and S_B, two kinds of adsorbing sites on octahedral Fe_3O_4 nanocrystals.

The different adsorption ability of these heavy metal atoms can also be observed from their adsorption structures. Figure 8 shows the optimized adsorbing structures of different heavy metal atoms on the surface of (100)-bound cubic Fe_3O_4 nanocrystals. The heavy metal atoms prefer to bind with two O atoms as well as one Fe atom. The distances of M−O are presented in the order of Cu−O (1.993 Å/1.969 Å) < Pb−O (2.356 Å/2.303 Å) ≈ Zn−O (2.567 Å/2.230 Å) < Cd−O (3.076 Å/2.932 Å) < Hg−O (3.374 Å/3.349 Å), which is not consistent with the order of heavy metal atom radii of Cu (1.17 Å) < Zn (1.25 Å) < Cd (1.48 Å) ≈ Hg (1.44 Å) ≈ Pb (1.47 Å). Obviously, the abnormal short distance Pb−O is presented, which is attributed to its strong adsorbing interaction with the surface of Fe_3O_4.

Similar phenomena can also be observed for metal atom adsorption on octahedral Fe_3O_4 nanocrystals exposed with (111) facets. The optimized adsorbing structures are shown in Figure 9; it can be seen that the heavy metal atoms prefer to adsorb on the hollow site of surface oxygen atoms. Such hollow adsorption sites can be further classified as S_A and S_B on the basis of whether or not there is a second layer Fe atom under

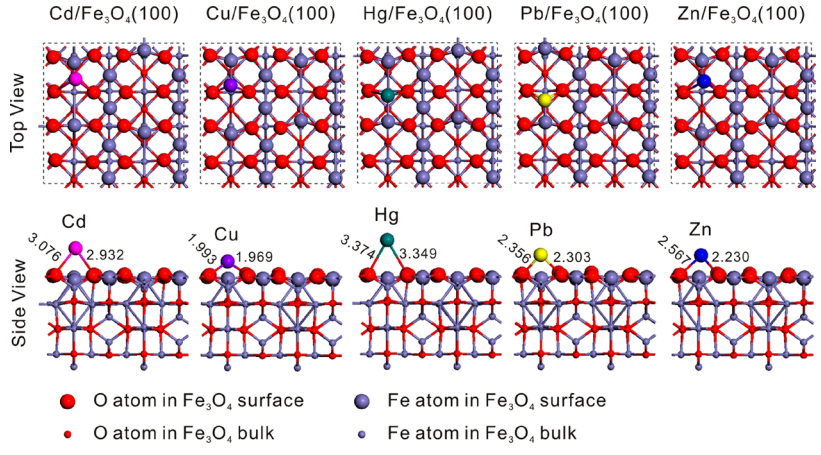

Figure 8. Top/side views of optimized geometric structures for adsorption states of heavy metal ions on cubic Fe_3O_4 nanocrystals exposed with (100) facets.

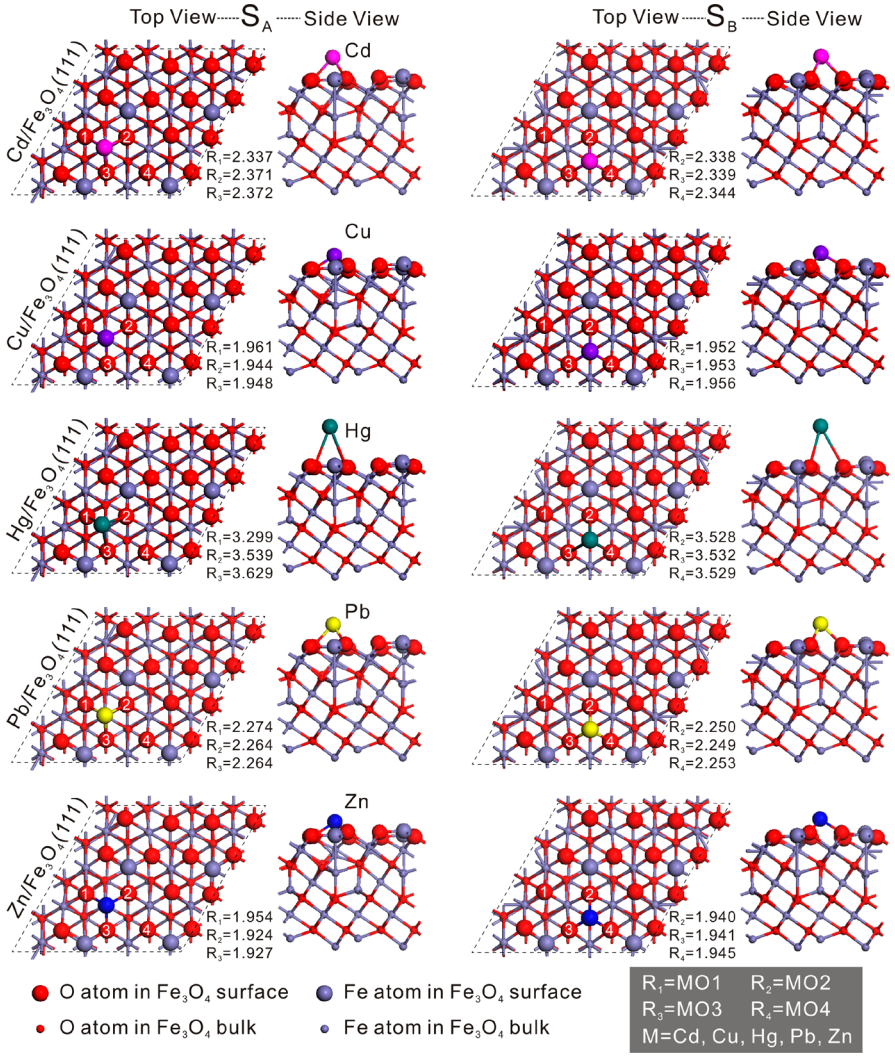

Figure 9. Top/side views of optimized geometric structures for adsorption states of heavy metal ions on octahedral Fe_3O_4 nanocrystals exposed with (111) facets. S_A and S_B, two kinds of adsorption sites of heavy metal ions on Fe_3O_4 (111) facets.

the hollow site. Compared with adsorption on the (100) facet where the heavy metal atom is coordinated by two O atoms and one Fe atom, the heavy metal atom adsorption on the (111) facets is coordinated by three O atoms. Thus, a strong adsorption on the (111) surface is expected because the binding of M−O is stronger than that of M−Fe. For example, the calculated adsorption energy of Pd atom on the (111) surface is −3.65 and −3.64 eV on S_A and S_B, respectively, which is ∼0.6 eV larger than that on the (100) facet. On the basis of the above calculation results, we can conclude that Pb adsorption on Fe_3O_4 (100) and (111) is much more favorable than the Cd, Cu, Hg, and Zn atoms. In addition, the facet of Fe_3O_4 affects the adsorption of heavy metal atoms. Metal atom adsorption on the (111) facet is much stronger than on the (100) facet because of the more adsorption site, as well as the large adsorption energy. These calculation results support our experimental observations very well and thus the best striping behaviors for Pb is well understood.

Detection of As(III). The above experimental and theoretical results perfectly indicate that octahedral Fe_3O_4 nanocrystals with higher adsorption energies and more adsorption sites toward heavy metal ions show much better electrochemical sensing performances and adsorption abilities in contrast to cubic Fe_3O_4 nanocrystals. To further check these results, their electrochemical stripping behaviors toward As(III) have been performed. Arsenic is a good model contaminant for further confirmation because it exhibits strong adsorption onto iron oxide (Fe_3O_4) nanocrystalline surfaces, and its interaction with iron oxides is strong.[44,50,51] It has been also demonstrated that the microspherical Fe_3O_4-RTIL (room temperature ionic liquid) composite modified screen-printed carbon electrode showed even better electrochemical performance than commonly used noble metals. Similar experimental processes were employed in the present work. Electrochemical characterization of the fabricated electrodes and their active electrode surfaces are shown in Figure S10 and S11, respectively (see the Supporting Information for details). Under the optimal experimental conditions, for cubic Fe_3O_4 nanocrystals-$[C_4dmim][NTf_2]$ modified SPE (Figure 10a), As(III) in a concentration range of 10 to 200 ppb was determined with the sensitivity of 1.08 $\mu A\ cm^{-2}\ ppb^{-1}$ and a correlation coefficient of 0.977. The lowest detectable concentration actually measured is 10 ppb. In contrast to bare SPE (1.04 $\mu A\ cm^{-2}\ ppb^{-1}$), (100)-bound cubic Fe_3O_4 nanocrystals almost do not contribute to the sensitivity and linear range. For octahedral Fe_3O_4 nanocrystals-$[C_4dmim][NTf_2]$ modified SPE (Figure

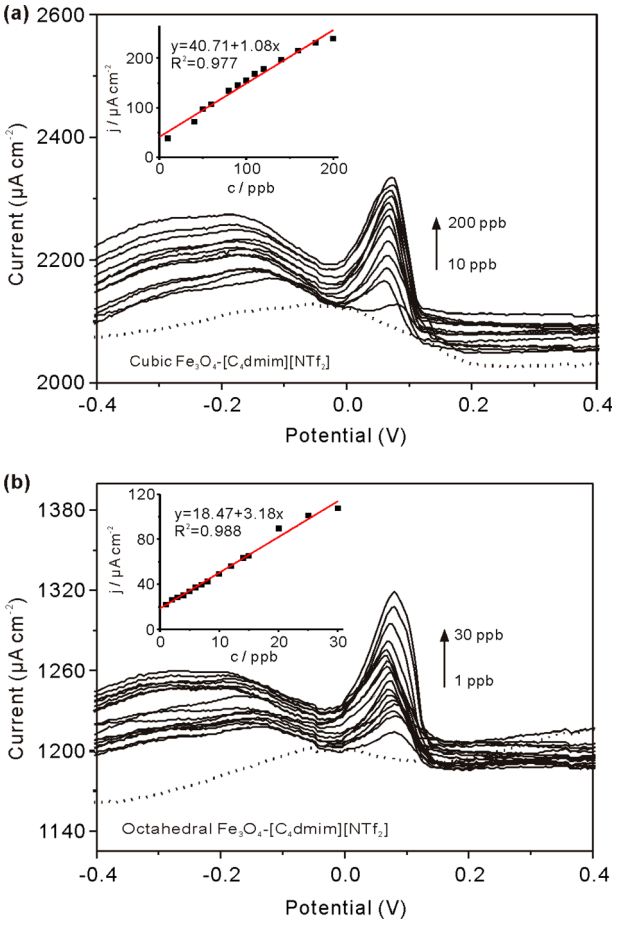

Figure 10. Typical SWASV response of (a) Fe_3O_4 cubes-[C_4dmim]-[NTf_2] and (b) Fe_3O_4 octahedrons-[C_4dmim][NTf_2] composite modified SPE for analysis of As(III) in different concentration ranges. Insets in panels a and b are corresponding linear calibration plots of peak current against As(III) concentrations, respectively. Supporting electrolyte, 0.1 M acetate buffer (pH 5.0); deposition potential, −0.5 V; deposition time, 120 s; amplitude, 25 mV; increment potential, 4 mV; frequency, 15 Hz. The dotted line refers to the baseline.

10b), the obtained sensitivity in a relatively low concentration range of 1−30 ppb is 3.18 μA cm^{-2} ppb^{-1}, which is about 3-fold that for cubic Fe_3O_4 nanocrystals-[C_4dmim][NTf_2] modified SPE. Furthermore, a higher correlation coefficient of 0.988 with a lower actually detectable concentration is down to 1 ppb. As seen from the sensitivity and linear range, the stripping behaviors of As(III) on (100)-bound cubic and (111)-bound octahedral Fe_3O_4 nanocrystals are facet-dependent. Undoubtedly, the greatly enhanced sensitivity is ascribed to the high adsorptivity of the Fe_3O_4 (111) facet toward As(III), which can accumulate more As(III) on the modified electrode surface. Finally, although the sensitivity of As(III) on (111)-bound octahedral Fe_3O_4 nanocrystals has no advantages by comparison with that of the Fe_3O_4 microsphere, it cannot affect our understanding about the impact of facet of nanocrystals on electrochemical stripping behaviors.

Currently, great efforts have been made on designing and fabricating the modified electrodes for electrochemical determination of As(III). Especially, a series of successful work aiming at detecting As(III) is obtained and corresponding results are shown in Table 2. Such trendy materials such as noble metal nanoparticles (Au, Ag, Pt, etc.) and organic and biological sensing materials are involved. Although the analytical performance of (111)-bound octahedral Fe_3O_4 nanocrystals is not the best, the results will guide us to find a new sensing interface (that is, metal oxide) toward As(III) in controlling the electrode morphology.

CONCLUSIONS

In the present work, we have demonstrated that Fe_3O_4 nanocrystals exposed with different facets present different electrochemical stripping behaviors toward heavy metal ions. Among all investigated heavy metal ions, Pb(II) is found to have the best stripping performances on both (100)- and (111)-bound Fe_3O_4 nanocrystals. (111)-bound octahedral Fe_3O_4 nanocrystals show a better electrochemical sensing performance than that of (100)-bound cubic Fe_3O_4 nanocrystals toward heavy metal ions including Zn(II), Cd(II), Pb(II), Cu(II), and Hg(II). The adsorption abilities of cubic and octahedral Fe_3O_4 nanocrystals were measured and in excellent agreement with electrochemical results. DFT calculations suggest that different stripping behaviors for heavy metal ions are attributed to their different adsorption ability on Fe_3O_4 nanocrystals. Furthermore, compared with Fe_3O_4 (100) facets, Fe_3O_4 (111) facets exhibit relatively larger adsorption energies and more adsorption sites, which may be the main reason accounting for the different electrochemical stripping and adsorption behaviors toward heavy metal ions. These studies

Table 2. Comparison of Electrochemical Performance of Nanomaterials Modified Electrodes for Voltammetric Determination of As(III)

electrode	electrolyte	linear range (ppb)	sensitivity (μA ppb^{-1})	ref
CNTs/leucine/Nafion-Pt electrode	0.1 M citrate buffer	1.489−149.8	0.36048	52
CNTs/amino acid-Pt electrode	0.1 M acetate buffer	0.0749−3.782	1.335	53
AgNPs/CT-GCE	1 M HNO_3	10−100	0.309	54
Cyt c-BDD	0.1 M PBS	0−750	0.00025	55
ERGO-AuNPs GCE	0.2 M HCl	0.75−375	0.16	56
Au(111)-like Au electrode	0.1 M PBS	9−1125	0.3636	57
AuNPs-GCE	0.5 M H_2SO_4	1.5−225	2.69	58
Au/Pd GCE	0.1 M acetate buffer	1−25	0.172	59
Au-NEE	0.2 M HCl	0.2−6	65.57	60
Au/Te GCE	1 M HCl	0.1−10	6.35	61
(111)-bound octahedral Fe_3O_4-SPE	0.1 M acetate buffer	1−30	3.18	this work

Cyt c, cytochrome c; SWCNT, single-wall carbon nanotubes; SPE, screen-printed electrode; PBS, phosphate buffer solution; AuNPs, gold nanoparticles; GC, glassy carbon microspheres; ERGO, electroreduced graphene oxide.

reveal that the as-prepared Fe_3O_4 nanocrystals exhibit interesting facet-dependent electrochemical behaviors toward heavy metal ions. This work will contribute to a deep understanding of intrinsic electrochemical performance on a certain facet of nanocrystals and be favorable to develop their novel adsorbents toward heavy metal ions.

■ ASSOCIATED CONTENT

Supporting Information

SEM images of cubic and octahedral Fe_3O_4 nanocrystals prepared with different conditions (Figures S1−S3); XRD pattern and N_2 adsorption−desorption isotherms of cubic and octahedral Fe_3O_4 nanocrystals (Figures S4 and S5); cyclic voltammograms, Nyquist diagram of electrochemical impedance spectra, and scan rate study at cubic and octahedral Fe_3O_4 nanocrystals modified GCE (Figures S6 and S7); optimal experimental conditions (Figure S8); typical SWASV response of Pb(II) at cubic and octahedral Fe_3O_4 nanocrystals modified GCE (Figure S9); typical SWASV response of cubic and octahedral Fe_3O_4 nanocrystals modified GCE for individual determination of Zn(II), Cd(II), Cu(II), and Hg(II) (Figures S10 and S11); cyclic voltammograms and Nyquist diagram of electrochemical impedance spectra, and scan rate study at cubic and octahedral Fe_3O_4 nanocrystals modified SPE (Figures S12 and S13). This material is available free of charge via the Internet at http://pubs.acs.org.

■ AUTHOR INFORMATION

Corresponding Author

*X. J. Huang. E-mail: xingjiuhuang@iim.ac.cn. Tel.: +86-551-5591142. Fax: +86-551-5592420.

Author Contributions

⊥These authors contributed equally to this work.

Notes

The authors declare no competing financial interest.

■ ACKNOWLEDGMENTS

This work was supported by the National Key Scientific Program-Nanoscience and Nanotechnology (2011CB933700). X.J.H. acknowledges the CAS Institute of Physical Science, University of Science and Technology of China (2012FXCX008), for financial support. The computations were performed in the Supercomputer Center of East China Normal University.

■ REFERENCES

(1) Battistel, D.; Baldi, F.; Marchetto, D.; Gallo, M.; Daniele, S. A Rapid Electrochemical Procedure for the Detection of Hg(0) Produced by Mercuric-Reductase: Application for Monitoring Hg-Resistant Bacteria Activity. *Environ. Sci. Technol.* **2012**, *46*, 10675−10681.

(2) Liu, G. D.; Lin, Y. Y.; Wu, H.; Lin, Y. Voltammetric Detection of Cr(VI) with Disposable Screen-Printed Electrode Modified with Gold Nanoparticles. *Environ. Sci. Technol.* **2007**, *41*, 8129−8134.

(3) Koehler, F. M.; Rossier, M.; Waelle, M.; Athanassiou, E. K.; Limbach, L. K.; Grass, R. N.; Gunther, D.; Stark, W. J. Magnetic EDTA: Coupling Heavy Metal Chelators to Metal Nanomagnets for Rapid Removal of Cadmium, Lead and Copper from Contaminated Water. *Chem. Commun. (Cambridge, U. K.)* **2009**, 4862−4864.

(4) Yantasee, W.; Lin, Y. H.; Hongsirikarn, K.; Fryxell, G. E.; Addleman, R.; Timchalk, C. Electrochemical Sensors for the Detection of Lead and Other Toxic Heavy Metals: The Next Generation of Personal Exposure Biomonitors. *Environ. Health Perspect.* **2007**, *115*, 1683−1690.

(5) Dai, X.; Nekrassova, O.; Hyde, M. E.; Compton, R. G. Anodic Stripping Voltammetry of Arsenic(III) Using Gold Nanoparticle-Modified Electrodes. *Anal. Chem.* **2004**, *76*, 5924−5929.

(6) Hocevar, S. B.; Svancara, I.; Ogorevc, B.; Vytras, K. Antimony Film Electrode for Electrochemical Stripping Analysis. *Anal. Chem.* **2007**, *79*, 8639−8643.

(7) Aragay, G.; Pons, J.; Merkoci, A. Recent Trends in Macro-, Micro-, and Nanomaterial-Based Tools and Strategies for Heavy-Metal Detection. *Chem. Rev.* **2011**, *111*, 3433−3458.

(8) van Staden, J. F.; Matoetoe, M. C. Simultaneous Determination of Copper, Lead, Cadmium and Zinc Using Differential Pulse Anodic Stripping Voltammetry in a Flow System. *Anal. Chim. Acta* **2000**, *411*, 201−207.

(9) Guo, Z.; Wei, Y.; Yang, R.; Liu, J. H.; Huang, X. J. Hydroxylation/Carbonylation Carbonaceous Microspheres: A Route without the Need for an External Functionalization to a "Hunter" of Lead(II) for Electrochemical Detection. *Electrochim. Acta* **2013**, *87*, 46−52.

(10) Lin, M.; Cho, M.; Choe, W. S.; Yoo, J. B.; Lee, Y. Polypyrrole Nanowire Modified with Gly-Gly-His Tripeptide for Electrochemical Detection of Copper Ion. *Biosens. Bioelectron.* **2010**, *26*, 940−945.

(11) Ganjali, M. R.; Motakef-Kazami, N.; Faridbod, F.; Khoee, S.; Norouzi, P. Determination of Pb^{2+} Ions by a Modified Carbon Paste Electrode Based on Multi-Walled Carbon Nanotubes (MWCNTs) and Nanosilica. *J. Hazard. Mater.* **2010**, *173*, 415−419.

(12) Yi, H. C. Anodic Stripping Voltammetric Determination of Mercury Using Multi-Walled Carbon Nanotubes Film Coated Glassy Carbon Electrode. *Anal. Bioanal. Chem.* **2003**, *377*, 770−774.

(13) Li, J.; Guo, S. J.; Zhai, Y. M.; Wang, E. K. Nafion-Graphene Nanocomposite Film as Enhanced Sensing Platform for Ultrasensitive Determination of Cadmium. *Electrochem. Commun.* **2009**, *11*, 1085−1088.

(14) Shen, L.; Chen, Z.; Li, Y. H.; He, S. L.; Xie, S. B.; Xu, X. D.; Liang, Z. W.; Meng, X.; Li, Q.; Zhu, Z. W.; Li, M. X.; Le, X. C.; Shao, Y. H. Electrochemical DNAzyme Sensor for Lead Based on Amplification of DNA-Au Bio-Bar Codes. *Anal. Chem.* **2008**, *80*, 6323−6328.

(15) Yang, X. R.; Xu, J.; Tang, X. M.; Liu, H. X.; Tian, D. B. A Novel Electrochemical DNAzyme Sensor for the Amplified Detection of Pb^{2+} Ions. *Chem. Commun. (Cambridge, U. K.)* **2010**, *46*, 3107−3109.

(16) Wang, L.; Xu, W. H.; Yang, R.; Zhou, T.; Hou, D.; Zheng, X.; Liu, J. H.; Huang, X. J. Electrochemical and Density Functional Theory Investigation on High Selectivity and Sensitivity of Exfoliated Nano-Zirconium Phosphate toward Lead(II). *Anal. Chem.* **2013**, *85*, 3984−3990.

(17) Wei, Y.; Liu, Z. G.; Yu, X. Y.; Wang, L.; Liu, J. H.; Huang, X. J. O_2-Plasma Oxidized Multi-Walled Carbon Nanotubes for Cd(II) and Pb(II) Detection: Evidence of Adsorption Capacity for Electrochemical Sensing. *Electrochem. Commun.* **2011**, *13*, 1506−1509.

(18) Zhao, Z. Q.; Chen, X.; Yang, Q.; Liu, J. H.; Huang, X. J. Selective Adsorption toward Toxic Metal Ions Results in Selective Response: Electrochemical Studies on a Polypyrrole/Reduced Graphene Oxide Nanocomposite. *Chem. Commun.* **2012**, *48*, 2180−2182.

(19) Cao, C. Y.; Cui, Z. M.; Chen, C. Q.; Song, W. G.; Cai, W. Ceria Hollow Nanospheres Produced by a Template-Free Microwave-Assisted Hydrothermal Method for Heavy Metal Ion Removal and Catalysis. *J. Phys. Chem. C* **2010**, *114*, 9865−9870.

(20) Cao, A. M.; Monnell, J. D.; Matranga, C.; Wu, J. M.; Cao, L. L.; Gao, D. Hierarchical Nanostructured Copper Oxide and Its Application in Arsenic Removal. *J. Phys. Chem. C* **2007**, *111*, 18624−18628.

(21) Yu, X. Y.; Luo, T.; Jia, Y.; Xu, R. X.; Gao, C.; Zhang, Y. X.; Liu, J. H.; Huang, X. J. Three-Dimensional Hierarchical Flower-Like Mg-Al-Layered Double Hydroxides: Highly Efficient Adsorbents for As(V) and Cr(VI) Removal. *Nanoscale* **2012**, *4*, 3466−3474.

(22) Jia, Y.; Yu, X. Y.; Luo, T.; Zhang, M. Y.; Liu, J. H.; Huang, X. J. Two-Step Self-Assembly of Iron Oxide into Three-Dimensional Hollow Magnetic Porous Microspheres and Their Toxic Ion Adsorption Mechanism. *Dalton Trans.* **2013**, *42*, 1921−1928.

(23) Yu, X. Y.; Xu, R. X.; Gao, C.; Luo, T.; Jia, Y.; Liu, J. H.; Huang, X. J. Novel 3D Hierarchical Cotton-Candy-Like CuO: Surfactant-Free Solvothermal Synthesis and Application in As(III) Removal. *ACS Appl. Mater. Interfaces* **2012**, *4*, 1954−1962.
(24) Wei, Y.; Gao, C.; Meng, F. L.; Li, H. H.; Wang, L.; Liu, J. H.; Huang, X. J. SnO_2/Reduced Graphene Oxide Nanocomposite for the Simultaneous Electrochemical Detection of Cadmium(II), Lead(II), Copper(II), and Mercury(II): An Interesting Favorable Mutual Interference. *J. Phys. Chem. C* **2012**, *116*, 1034−1041.
(25) Wei, Y.; Yang, R.; Yu, X. Y.; Wang, L.; Liu, J. H.; Huang, X. J. Stripping Voltammetry Study of Ultra-Trace Toxic Metal Ions on Highly Selectively Adsorptive Porous Magnesium Oxide Nanoflowers. *Analyst* **2012**, *137*, 2183−2191.
(26) Xu, R. X.; Yu, X. Y.; Gao, C.; Liu, J. H.; Compton, R. G.; Huang, X. J. Enhancing Selectivity in Stripping Voltammetry by Different Adsorption Behaviors: The Use of Nanostructured Mg-Al-Layered Double Hydroxides to Detect Cd(II). *Analyst* **2013**, *138*, 1812−1818.
(27) Gao, C.; Yu, X. Y.; Xiong, S. Q.; Liu, J. H.; Huang, X. J. Electrochemical Detection of Arsenic(III) Completely Free from Noble Metal: Fe_3O_4 Microspheres-Room Temperature Ionic Liquid Composite Showing Better Performance than Gold. *Anal. Chem.* **2013**, *85*, 2673−2680.
(28) Zhong, L. S.; Hu, J. S.; Cao, A. M.; Liu, Q.; Song, W. G.; Wan, L. J. 3D Flowerlike Ceria Micro/Nanocomposite Structure and Its Application for Water Treatment and CO Removal. *Chem. Mater.* **2007**, *19*, 1648−1655.
(29) Fan, W. H.; Wang, X. L.; Cui, M. M.; Zhang, D. F.; Zhang, Y.; Yu, T.; Guo, L. Differential Oxidative Stress of Octahedral and Cubic Cu_2O Micro/Nanocrystals to Daphnia Magna. *Environ. Sci. Technol.* **2012**, *46*, 10255−10262.
(30) Jiang, Z. Y.; Kuang, Q.; Xie, Z. X.; Zheng, L. S. Syntheses and Properties of Micro/Nanostructured Crystallites with High-Energy Surfaces. *Adv. Funct. Mater.* **2010**, *20*, 3634−3645.
(31) Tao, A. R.; Habas, S.; Yang, P. Shape Control of Colloidal Metal Nanocrystals. *Small* **2008**, *4*, 310−325.
(32) Geng, B.; Fang, C.; Zhan, F.; Yu, N. Synthesis of Polyhedral $ZnSnO_3$ Microcrystals with Controlled Exposed Facets and Their Selective Gas-Sensing Properties. *Small* **2008**, *4*, 1337−1343.
(33) Wu, Z.; Jiang, L.; Chen, H.; Xu, C.; Wang, X. Synthesis of Folding Flake-Like CuO Sub-Microstructure and Its Application on Mercury (II) Sensor. *J. Mater. Sci.: Mater. Electron.* **2011**, *23*, 858−864.
(34) Hu, L.; Sun, K.; Peng, Q.; Xu, B.; Li, Y. Surface Active Sites on Co_3O_4 Nanobelt and Nanocube Model Catalysts for CO Oxidation. *Nano Res.* **2010**, *3*, 363−368.
(35) Liu, S. H.; Lu, F.; Xing, R. M.; Zhu, J. J. Structural Effects of Fe_3O_4 Nanocrystals on Peroxidase-Like Activity. *Chem.—Eur. J.* **2011**, *17*, 620−625.
(36) Zhao, Y.; Pan, F.; Li, H.; Niu, T.; Xu, G.; Chen, W. Facile Synthesis of Uniform Alpha-Fe_2O_3 Crystals and Their Facet-Dependent Catalytic Performance in the Photo-Fenton Reaction. *J. Mater. Chem. A* **2013**, *1*, 7242.
(37) Wang, S.; Zhao, L.; Wang, W.; Zhao, Y.; Zhang, G.; Ma, X.; Gong, J. Morphology Control of Ceria Nanocrystals for Catalytic Conversion of CO_2 with Methanol. *Nanoscale* **2013**, *5*, 5582−5588.
(38) Xu, T.; Zhou, X.; Jiang, Z. Y.; Kuang, Q.; Xie, Z. X.; Zheng, L. S. Syntheses of Nano/Submicrostructured Metal Oxides with All Polar Surfaces Exposed via a Molten Salt Route. *Cryst. Growth Des.* **2009**, *9*, 192−196.
(39) Fan, D. B.; Thomas, P. J.; O'Brien, P. Pyramidal Lead Sulfide Crystallites with High Energy (113) Facets. *J. Am. Chem. Soc.* **2008**, *130*, 10892−10894.
(40) Yu, X.; Chen, K. A Facile Surfactant-Free Fabrication of Single-Crystalline Truncated Fe_3O_4 Cubes. *Mater. Sci. Eng., B* **2011**, *176*, 750−755.
(41) Kresse, G.; Furthmuller, J. Efficiency of Ab-Initio Total Energy Calculations for Metals and Semiconductors Using a Plane-Wave Basis Set. *Comput. Mater. Sci.* **1996**, *6*, 15−50.
(42) Kresse, G.; Furthmüller, J. Efficient Iterative Schemes for Ab Initio Total-Energy Calculations Using a Plane-Wave Basis Set. *Phys. Rev. B* **1996**, *54*, 11169−11186.
(43) Perdew, J. P.; Burke, K.; Ernzerhof, M. Generalized Gradient Approximation Made Simple. *Phys. Rev. Lett.* **1996**, *77*, 3865−3868.
(44) Yavuz, C. T.; Mayo, J. T.; Yu, W. W.; Parkash, A.; Falkner, J. C.; Yean, S.; Cong, L.; Shipley, H. J.; Kan, A.; Tomson, M.; Natelson, D.; Colvin, V. L. Low-Field Magnetic Separation of Monodisperse Fe_3O_4 Nanocrystals. *Science* **2006**, *314*, 964−968.
(45) Zhao, L.; Duan, L. Uniform Fe_3O_4 Octahedra with Tunable Edge Length - Synthesis by a Facile Polyol Route and Magnetic Properties. *Eur. J. Inorg. Chem.* **2010**, *2010*, 5635−5639.
(46) Tang, Q.; Zhou, Z.; Shen, P. Are MXenes Promising Anode Materials for Li Ion Batteries? Computational Studies on Electronic Properties and Li Storage Capability of Ti_3C_2 and $Ti_3C_2X_2$ (X = F, OH) Monolayer. *J. Am. Chem. Soc.* **2012**, *134*, 16909−16916.
(47) Ding, Y.; Fan, F. R.; Tian, Z. Q.; Wang, Z. L. Sublimation-Induced Shape Evolution of Silver Cubes. *Small* **2009**, *5*, 2812−2815.
(48) Hu, L. H.; Peng, Q.; Li, Y. D. Selective Synthesis of Co_3O_4 Nanocrystal with Different Shape and Crystal Plane Effect on Catalytic Property for Methane Combustion. *J. Am. Chem. Soc.* **2008**, *130*, 16136−16139.
(49) Zhou, K. B.; Wang, X.; Sun, X. M.; Peng, Q.; Li, Y. D. Enhanced Catalytic Activity of Ceria Nanorods from Well-Defined Reactive Crystal Planes. *J. Catal.* **2005**, *229*, 206−212.
(50) Feng, L. Y.; Cao, M. H.; Ma, X. Y.; Zhu, Y. S.; Hu, C. W. Superparamagnetic High-Surface-Area Fe_3O_4 Nanoparticles as Adsorbents for Arsenic Removal. *J. Hazard. Mater.* **2012**, *217*, 439−446.
(51) Jiang, W.; Chen, X. B.; Niu, Y. J.; Pan, B. C. Spherical Polystyrene-Supported Nano-Fe_3O_4 of High Capacity and Low-Field Separation for Arsenate Removal from Water. *J. Hazard. Mater.* **2012**, *243*, 319−325.
(52) Daud, N.; Yusof, N. A.; Tee, T. W.; Abdullah, A. H. Electrochemical Sensor for As(III) Utilizing CNTs/Leucine/Nafion Modified Electrode. *Int. J. Electrochem. Sci.* **2012**, *7*, 175−185.
(53) Yusof, N. A.; Daud, N.; Tee, T. W.; Abdullah, A. H. Electrocatalytic Characteristic of Carbon Nanotubes/Glutamine/Nafion Modified Platinum Electrode in Development of Sensor for Determination of As(III). *Int. J. Electrochem. Sci.* **2011**, *6*, 2385−2397.
(54) Prakash, S.; Chakrabarty, T.; Singh, A. K.; Shahi, V. K. Silver Nanoparticles Built-In Chitosan Modified Glassy Carbon Electrode for Anodic Stripping Analysis of As(III) and Its Removal from Water. *Electrochim. Acta* **2012**, *72*, 157−164.
(55) Fuku, X.; Iftikar, F.; Hess, E.; Iwuoha, E.; Baker, P. Cytochrome c Biosensor for Determination of Trace Levels of Cyanide and Arsenic Compounds. *Anal. Chim. Acta* **2012**, *730*, 49−59.
(56) Liu, Y.; Huang, Z.; Xie, Q.; Sun, L.; Gu, T.; Li, Z.; Bu, L.; Yao, S.; Tu, X.; Luo, X.; Luo, S. Electrodeposition of Electroreduced Graphene Oxide-Au Nanoparticles Composite Film at Glassy Carbon Electrode for Anodic Stripping Voltammetric Analysis of Trace Arsenic(III). *Sens. Actuators, B* **2013**, *188*, 894−901.
(57) Rahman, M. R.; Okajima, T.; Ohsaka, T. Selective Detection of As(III) at the Au(111)-Like Polycrystalline Gold Electrode. *Anal. Chem.* **2010**, *82*, 9169−9176.
(58) Gu, T.; Bu, L.; Huang, Z.; Liu, Y.; Tang, Z.; Liu, Y.; Huang, S.; Xie, Q.; Yao, S.; Tu, X.; Luo, X.; Luo, S. Dual-Signal Anodic Stripping Voltammetric Determination of Trace Arsenic(III) at a Glassy Carbon Electrode Modified with Internal-Electrolysis Deposited Gold Nanoparticles. *Electrochem. Commun.* **2013**, *33*, 43−46.
(59) Lan, Y.; Luo, H.; Ren, X.; Wang, Y.; Wang, L. Glassy Carbon Electrode Modified with Citrate Stabilized Gold Nanoparticles for Sensitive Arsenic(III) Detection. *Anal. Lett.* **2012**, *45*, 1184−1196.
(60) Mardegan, A.; Scopece, P.; Lamberti, F.; Meneghetti, M.; Moretto, L. M.; Ugo, P. Electroanalysis of Trace Inorganic Arsenic with Gold Nanoelectrode Ensembles. *Electroanalysis* **2012**, *24*, 798−806.
(61) Wang, D.; Zhao, Y.; Jin, H.; Zhuang, J.; Zhang, W.; Wang, S.; Wang, J. Synthesis of Au-Decorated Tripod-Shaped Te Hybrids for

Applications in the Ultrasensitive Detection of Arsenic. *ACS Appl. Mater. Interfaces* **2013**, *5*, 5733−5740.